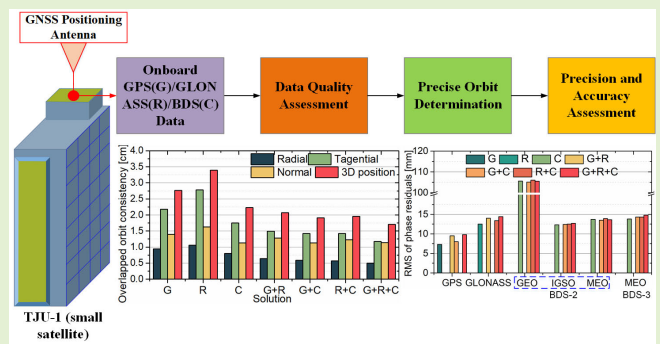


High-Precision Orbit Determination of the Small TJU-1 Satellite Using GPS, GLONASS, and BDS

Xuwen Gong¹, Xingxing Li¹, Pengcheng Wang, Qingyun Wang¹, Fuhong Wang, Jizhang Sang, and Shuaihe Gao¹

Abstract—Tianjin University-1 (TJU-1) is a small low-Earth-orbiting (LEO) meteorological satellite equipped with a multi-global navigation satellite system (GNSS) receiver that provides the dual-frequency pseudorange and carrier-phase measurements from Global Positioning System (GPS), Global Navigation Satellite System (GLONASS), and BeiDou Navigation Satellite System (BDS), including BDS-2 and BDS-3. In this contribution, the quality of GNSS data during the period of 2022/31–2022/37 is assessed, and the precise orbit determination (POD) based on the onboard GNSS data is conducted. Assessing the pseudorange measurement accuracy, it reveals that the GPS and BDS-3 are comparable, followed by BDS-2, and GLONASS the worst. The POD experiments demonstrate that the orbit precision of all single-GNSS solutions is almost at an equivalent level of 2.2–3.4 cm, in terms of the overlapped orbit consistency, and the GPS-based solution is slightly worse than the BDS-based one and the GLONASS-based one is worse than other two. According to the orbit differences between different solutions, the orbit accuracy of single-GNSS solutions is inferred to be at the level of about 4.7–6.2 cm. With the multi-GNSS fusion, the precision and inferred accuracy of orbits could be improved significantly to 1.7–2.1 cm and about 1.7–3.7 cm, respectively. Furthermore, the root mean square (RMS) of posteriori carrier-phase residuals for all the IGSO/MEO satellites is at the level of 7–15 mm in different single-GNSS and multi-GNSS fusion solutions. These performances have fully demonstrated that the centimeter-level POD is easily achievable for small LEO satellites by using the multi-GNSS receiver.

Index Terms—Global navigation satellite system (GNSS) data quality, multi-GNSS fusion, precise orbit determination (POD), precision and accuracy, Tianjin University-1 (TJU-1).



Manuscript received 12 April 2023; accepted 28 April 2023. Date of publication 9 May 2023; date of current version 14 June 2023. This work was supported in part by the China Postdoctoral Science Foundation under Grant 2021T140520 and Grant 2020M682479, in part by the Key Laboratory of Aerospace Environment and Geodesy, Ministry of Education, Wuhan University under Grant 21-02-02, in part by the State Key Laboratory of Satellite Navigation System and Equipment Technology, Shijiazhuang, Hebei, China, under Grant CEPNT-2021KF-10, in part by the National Science Foundation of Hubei Province, China, under Grant 2020CFA002, in part by the Science and Technology Plan Project of Tianjin Province under Grant 22ZYQYGX00060, in part by the National Natural Science Foundation of China under Grant 12273045, in part by the “Light of West China” Program of Chinese Academy of Sciences under Grant E016YR1R, and in part by the Shanxi Provincial Talents Plan under Grant E039SB1K. The associate editor coordinating the review of this article and approving it for publication was Prof. Yulong Huang. (Corresponding author: Xuwen Gong.)

Xuwen Gong and Shuaihe Gao are with the National Time Service Center, Chinese Academy of Sciences, Xi'an 710600, China (e-mail: xwgong@sigg.whu.edu.cn; gaoshuaihe@nsc.ac.cn).

Xingxing Li, Qingyun Wang, Fuhong Wang, and Jizhang Sang are with the School of Geodesy and Geomatics, Wuhan University, Wuhan 430079, China (e-mail: xxli@sigg.whu.edu.cn; qywang@whu.edu.cn; fhwang@sigg.whu.edu.cn; jzhsang@sigg.whu.edu.cn).

Pengcheng Wang is with Tianjin Yanyao Aerospace Technology Company, Ltd., Tianjin 300308, China (e-mail: wpchn@163.com).

Digital Object Identifier 10.1109/JSEN.2023.3272923

I. INTRODUCTION

SINCE America's Global Positioning System (GPS) was applied for the orbit determination (OD) of low-Earth-orbiting (LEO) satellites in the 1980s [1], precise orbit determination (POD) using onboard data from global navigation satellite system (GNSS) has gradually become one of the mainstream OD techniques for LEO satellites, due to its global coverage, abundant observations, high-precision, and low cost [2]. Over the past decades, GPS receivers have been widely applied in the POD of multifarious LEO satellites from the field of gravity, ocean, meteorology, resource, remote sensing, and so on, such as CHAMP [3], GRACE [4], GOCE [5], JASON [6], MetOp [7], ZY-3 [8], SWARM [9], and Sentinel [10]. A lot of studies have fully verified that the centimeter-level orbit precision and accuracy are easily achievable for LEO POD by using GPS receivers [11], [12], [13], [14], [15], [16]. With the recent developments or upgrades of multiple GNSS constellations, such as China's BeiDou Navigation Satellite System (BDS), Russia's Global Navigation Satellite System (GLONASS), and Europe's Galileo Navigation Satellite System (Galileo) [17],

the multi-GNSS receivers become practicable and available for space applications [18]. Therefore, some multi-GNSS receivers that could observe GPS and BDS-2, BDS-3, or Galileo signals have been carried onboard a series of LEO satellites, such as LINGQIAO [19], FY-3C [20], FY-3D [21], Luojia-1A [22], Tianping-1B [23], and Sentinel-6A [24]. Various studies have demonstrated the centimeter-level POD based on BDS-3/Galileo and the higher availability and reliability with multi-GNSS fusion are obtainable [23], [24], [25], [26].

The modern small LEO satellite not only denotes the satellite with a small size and mass in the physical sense (≤ 100 kg) but also represents a tight combination that integrates various commercial microelectronic devices, capable of sophisticated functions with high utility in a fraction of the volume, mass, cost, and timescales [27]. For a large number of small LEO satellites, a multi-GNSS receiver should be one of the most portable and integrable sensors for high-precision orbit determination. In fact, several literatures have studied the POD of some small LEO satellites, such as APOD-A [28], Luojia-1A [26], and Tianping-1B [23], and the orbit accuracy at decimeter to centimeter level has been obtained based on GPS, BDS, or GPS/BDS fusion. Therefore, it is necessary to perform further research about the POD of small satellites based on other unexplored GNSS constellations, such as GLONASS or more GNSS fusion, which is of important significance to promote the application of multi-GNSS for small satellites.

The Tianjin University-1 (TJU-1) satellite, manufactured by Tianjin Yunyao Aerospace Technology Company, Ltd., Tianjin, China, is a small meteorological satellite launched on December 7, 2021, aiming at global atmosphere and ionosphere detection, weather forecast, and short-term earthquake prediction. It flies on a sun-synchronous orbit with an altitude of about 500 km and an inclination of 97.4° . Usually, precise orbits at subdecimeter or centimeter level are necessary to generate precise occultation products for LEO satellites [29]. The TJU-1 satellite is equipped with a multi-GNSS receiver that could provide dual-frequency pseudorange and carrier-phase measurements from GPS, GLONASS, and BDS. The BDS includes the early regional BDS-2 constellation and the new generation BDS-3 constellation. The TJU-1 satellite and its high-precision orbit determination will be treated as the research target in this contribution. In theory, there is no essential difference between the basic POD methods of small LEO satellites and those of large satellites. Therefore, this contribution mainly focuses on the relevant issues of multi-GNSS data processing in POD, including the comparison of multi-GNSS data quality, the analysis about appropriate strategies and refined processing methods for orbit determination, and the in-depth assessment of final orbit precision and accuracy.

In the following text, the GNSS data quality of the receiver will be analyzed in detail first, in terms of the tracking performance of GNSS signals, the number of available GNSS satellites, and the pseudorange measurement accuracy. Then, the detailed POD strategies will be described, as well as some important disposals in POD processing. Meanwhile, the phase center offset (PCO) and phase center variation (PCV)

of the positioning antenna will be estimated and its influence on orbit determination is analyzed, so as to obtain a more precise PCO/PCV correction for POD. Afterward, a series of POD experiments based on different single-GNSS or multi-GNSS fusion are carried out, and an elaborate assessment of POD precision and accuracy is performed from some aspects, including the overlapped orbit consistency, the posteriori carrier-phase residuals, and the comparisons between different solutions. Of course, it should be noted that the TJU-1 satellite is not equipped with the laser retro reflector, so no satellite laser range (SLR) data are available to validate the external POD accuracy. Finally, some summaries and conclusions are made.

II. GNSS DATA QUALITY

GNSS receivers often show different observation characteristics for different GNSSs on different satellite platforms, which would affect the multi-GNSS-based POD solutions, the POD strategies, and the final orbit precision and accuracy. Therefore, the quality assessment of onboard GNSS data is essential before performing the POD. In consideration of the influence of small satellite platform, this section will evaluate the quality of the onboard GNSS data collected by the triple-constellation GNSS receiver based on the tracking performance of GNSS signals, the analysis of available GNSS satellites, and the pseudorange measurement accuracy.

A. Tracking Performance

The real-time navigation research of the TJU-1 satellite using GNSS broadcast ephemeris has been conducted, and information about the satellite and receiver has been detailed in the literature [30]. Readers are referred to this reference for more details. It is important to reiterate that the receiver can observe GPS L1/L2, GLONASS G1/G2, and BDS B1I/B3I signals, and GPS/GLONASS and BDS signals are acquired and tracked by two separate processing units. Therefore, the coarse adjustments of the receiver clocks for the generation of raw GPS/GLONASS and BDS measurements are not consistent, which requires estimating separate receiver clock offsets for GPS/GLONASS and BDS in multi-GNSS fusion processing.

The carrier-to-noise density ratio (C/N_0) is the ratio between the signal power and the noise power density, which could express the tracking performance of GNSS signals directly and reflect the accuracy of GNSS code measurements to a certain extent. In general, when other conditions are constant, the larger the C/N_0 is, the higher the code measurement accuracy [23]. The average C/N_0 versus elevation for each type of GNSS satellite is plotted in Fig. 1. It shows that the higher the elevation angle is, the larger the average C/N_0 and vice versa. The receiver is able to attain the crest and peak average C/N_0 values of 35 and 50 dB-Hz, respectively. It can also be observed that the L1 signal has a higher C/N_0 than the L2 signal for GPS, while G1 and B1I signals have lower C/N_0 than G2 and B3I signals for GLONASS and BDS-2 MEO, respectively. In addition, for BDS-2 GEO/IGSO and BDS-3 MEO, the average C/N_0 of the B3I signal is slightly larger than that of the B1I signal at elevation angles below

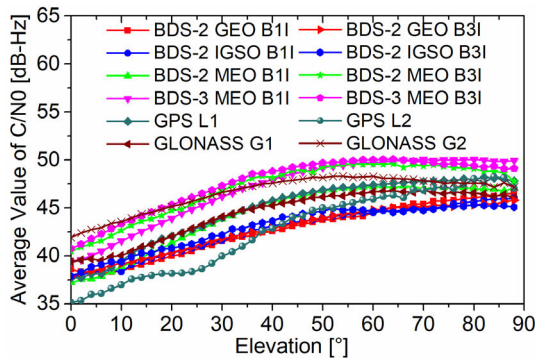


Fig. 1. Average carrier-to-noise ratios on different elevation angles for BDS-2 GEO, BDS-2 IGSO, BDS-2 MEO, BDS-3 MEO, GPS, and GLONASS.

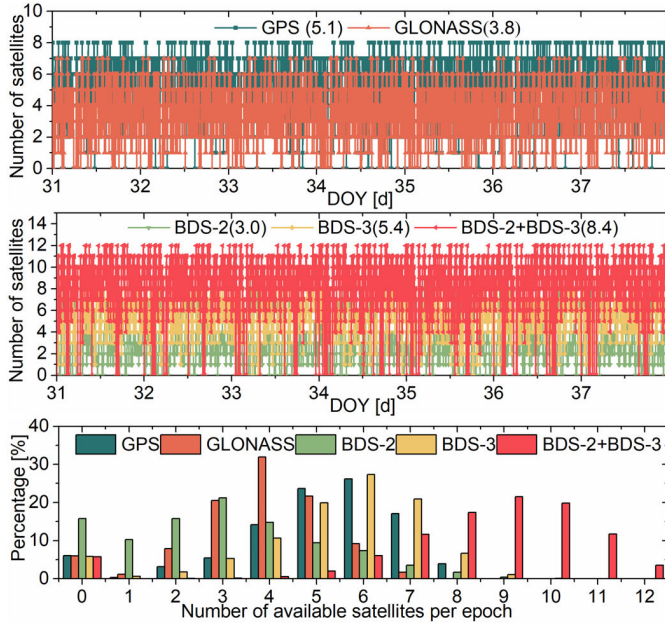


Fig. 2. Number of available GPS/GLONASS satellites (top) and BDS-2/BDS-3 satellites (middle) with the average number in the bracket, and the relationship between the time percentage and the number of available satellites (bottom).

60°, while the opposite is true at elevation angles above 65°. More significantly, the average C/N0 of B1I and B3I signals for BDS-3 MEO is notably larger than those for BDS-2 at different angles, which means the higher observation qualities for BDS-3 in comparison with BDS-2.

B. Available GNSS Satellites

An available GNSS satellite at an epoch is defined as one for which both the pseudorange and carrier-phase dual-frequency measurements are simultaneously available for POD processing. The availability of each type of GNSS satellite from 2022/31 to 2022/37 is shown in Fig. 2. It is clearly seen from the top and middle subgraphs that BDS-3 has the most available satellites for the receiver with the average number of 5.4, followed by GPS of 5.1 and GLONASS of 3.8, and the regional BDS-2 the fewest. According to the statistics in the bottom subgraph, BDS-3 could be available with four or more satellites in 86.5% of the time, GPS in 85.0%, and GLONASS and regional BDS-2 in 64.5% and 37.0%, respectively. Of course, for the whole BDS constellation (BDS-2 +

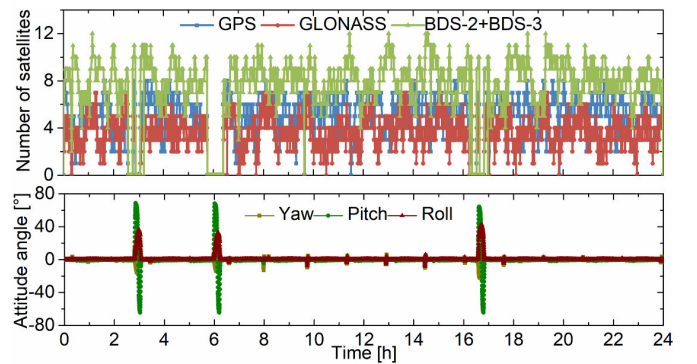


Fig. 3. Variations in the number of available GNSS satellites (top) and the three attitude angles (bottom) on 2022/31.

BDS-3), the average number of available satellites is up to 8.4, and in 94.1% of the time 4 or more BDS satellites could be used. Therefore, it can be concluded that the whole BDS achieves the best availability, followed by BDS-3, GPS, and GLONASS, and BDS-2 the worst.

What is noteworthy is that the number curves in Fig. 2 have displayed clearly that there is no satellite available at many epochs, and the time percentage statistics also show that there are no available BDS-3, GPS, GLONASS, and BDS-2 satellites in 5.9%, 6.1%, 6.0%, and 15.8% of the time, respectively. Even for BDS-2 + BDS-3, there is still 5.8% of the time without any usable satellite. This poor continuity and availability relate directly to the attitude adjustments of the TJU-1 satellite. Fig. 3 shows the number of available GNSS satellites at each epoch on 2022/31 and the corresponding variations of the three attitude angles (yaw, pitch, and roll). As can be seen clearly, the large-scale attitude adjustments with maximum orientation changes of $\pm 70^\circ$ occur in three periods, i.e., the period from 2.58 to 3.07 h, the one from 5.75 to 6.39 h, and the one from 16.35 to 16.84 h. It has been confirmed that the attitude adjustments with such large-scale orientation change are to facilitate the downlink transmission of onboard data from various payloads. During these periods, GNSS signals are disturbed seriously or even completely interrupted; thus, few or no GNSS satellites are available for the POD. According to the statistics, there are three such interrupted periods each day for the TJU-1 satellite. This indicates that the signal tracking is relatively unstable for the miniature GNSS receiver onboard the attitude-adjusting small satellite platform.

C. Pseudorange Measurement Accuracy

Since the noise and multipath error of carrier-phases are always much lower than those of pseudoranges by 2–3 orders of magnitude, the combinations (M_1, M_2) could be used to compute the pseudorange noise and multipath error [3]

$$\begin{cases} M_1 = -\frac{\alpha^2 + 1}{\alpha^2 - 1} \lambda_1 \varphi_1 + \frac{2}{\alpha^2 - 1} \lambda_2 \varphi_2 + P_1 \\ \quad = B_1 + D_1 + M P_1 + \varepsilon_1 \\ M_2 = -\frac{2\alpha^2}{\alpha^2 - 1} \lambda_1 \varphi_1 + \frac{\alpha^2 + 1}{\alpha^2 - 1} \lambda_2 \varphi_2 + P_2 \\ \quad = B_2 + D_2 + M P_2 + \varepsilon_2 \end{cases} \quad (1)$$

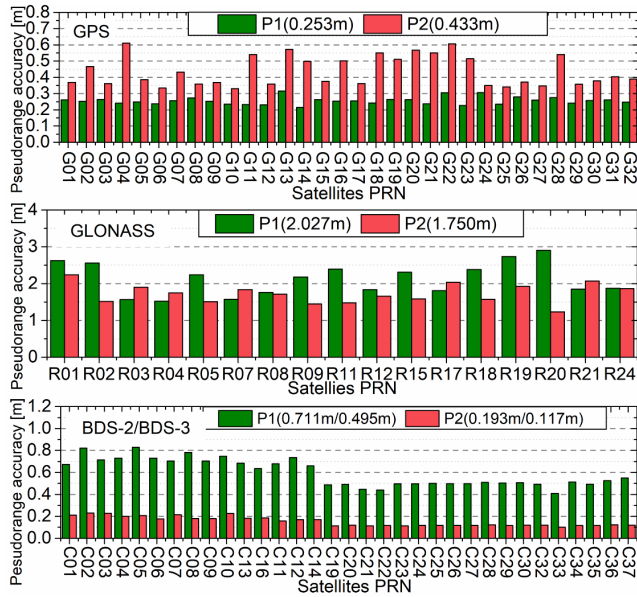


Fig. 4. Accuracy statistics (RMS) of pseudorange measurements for GPS (top), GLONASS (middle), and BDS-2/BDS-3 (bottom) satellites. The overall RMS is given in the bracket.

where (φ_1, φ_2) and (P_1, P_2) denote the dual-frequency carrier-phase and pseudorange measurements, respectively. (λ_1, λ_2) represents the wavelengths of the two frequencies, and $\alpha = \lambda_2/\lambda_1$ is the ratio between two wavelengths. (B_1, B_2) and (D_1, D_2) denote the combined ambiguity and hardware delay in the combinations, respectively. (MP_1, MP_2) and $(\varepsilon_1, \varepsilon_2)$ represent the MP_1/MP_2 multipath error and noise of the dual-frequency pseudorange measurements, respectively. In every continuous tracking arc without pseudorange outliers and carrier-phase cycle-slips, (B_1, B_2) and (D_1, D_2) should be constant, so the noise and multipath error $(MP_1 + \varepsilon_1, MP_2 + \varepsilon_2)$ could be extracted from (M_1, M_2) by subtracting the average values over each successive arc. The root mean square (RMS) statistics on the sequence of noise and multipath error $(MP_1 + \varepsilon_1, MP_2 + \varepsilon_2)$ could be used to represent the measurement accuracy of pseudoranges (P_1, P_2) . Fig. 4 shows the pseudorange measurement accuracy for each GNSS satellite, as well as the overall accuracy for each individual GNSS constellation. As can be observed, for GPS satellites, the accuracy of pseudorange P_1 is higher than that of pseudorange P_2 , while the opposite is true for GLONASS/BDS-2/BDS-3 satellites. In the case of the pseudorange P_1 , GPS shows the highest measurement accuracy of 0.253 m, followed by BDS-3 (C19–C37) of 0.495 m and BDS-2 (C01–C16) of 0.711 m, and GLONASS of 2.027 m the worst. Similarly, in the case of the pseudorange P_2 , the accuracies of BDS-2 and BDS-3 are 0.193 and 0.117 m, respectively, which are much higher than those of GPS and GLONASS with 0.443 and 1.750 m, respectively. One should note that BDS-3 signal shows more excellent quality compared with BDS-2 and GLONASS signals, and it is comparable to or even slightly better than the GPS signal in terms of (P_1, P_2) measurement accuracy. This performance is consistent with the analyses in the past research [31].

Fig. 5 shows the noises and multipath errors of pseudorange measurements (P_1, P_2) from GPS, GLONASS, BDS-2, and

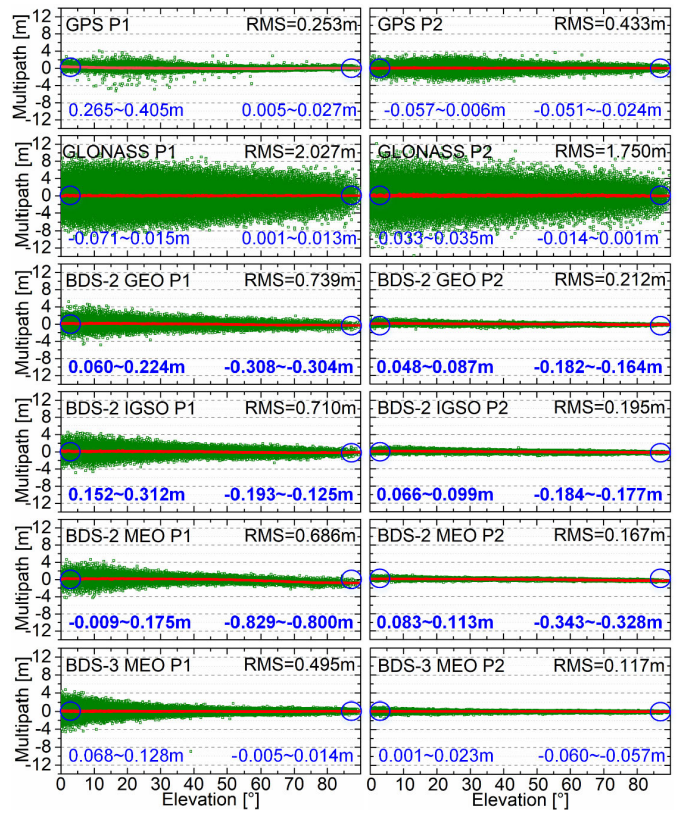


Fig. 5. Variation of pseudorange noise, multipath error, and the average value (red line) with an elevation angle for GPS, GLONASS, BDS-2 GEO, BDS-2 IGSO, BDS-2 MEO, and BDS-3 MEO. The average value is computed with a sliding window of 1000 points, and the blue circle and label in each panel represent the range of average values at the elevation from 0° to 5° (left) and from 85° to 90° (right).

BDS-3 satellites from 2022/31 to 2022/37, as well as their average values (red line), at different elevation angles. As can be seen clearly, the pseudorange noises and multipath errors of GLONASS are the largest in the range of ± 12 m, while those of GPS are much smaller in the range of ± 4 m and those of BDS are the smallest, in the range of ± 4 and ± 2 m for P_1 and P_2 , respectively. The pure pseudorange noise follows a normal distribution with a mean value of zero. Hence, the deviation of the average value curve (red line) from the zero axis is mainly caused by the multipath error. In other words, the more obvious the deviation from the zero axis, the more serious the multipath error. As can be observed clearly from the blue labels of the figure, the average values for GPS and GLONASS decrease with the increase of the elevation angle, and the average values are less than 0.05 m at the elevation from 85° to 90°. It indicates that there are no obvious multipath errors for GPS and GLONASS pseudoranges when the satellite elevations are high. However, the BDS-2 satellites exhibit the opposite variation pattern, namely, the multipath errors at high elevations are larger than those at low elevations, as the bold blue label shows in the figure. Especially for the pseudorange P_1 of BDS-2, the multipath error is up to 0.8 m at the elevation from 85° to 90°.

The distribution of MP_1/MP_2 could be revealed more clearly in the antenna azimuth–zenith maps, as shown in Fig. 6. For the zone with zenith angles below 30°, namely, elevation angles above 60°, the MP_1/MP_2 of GPS is close to 0 m,

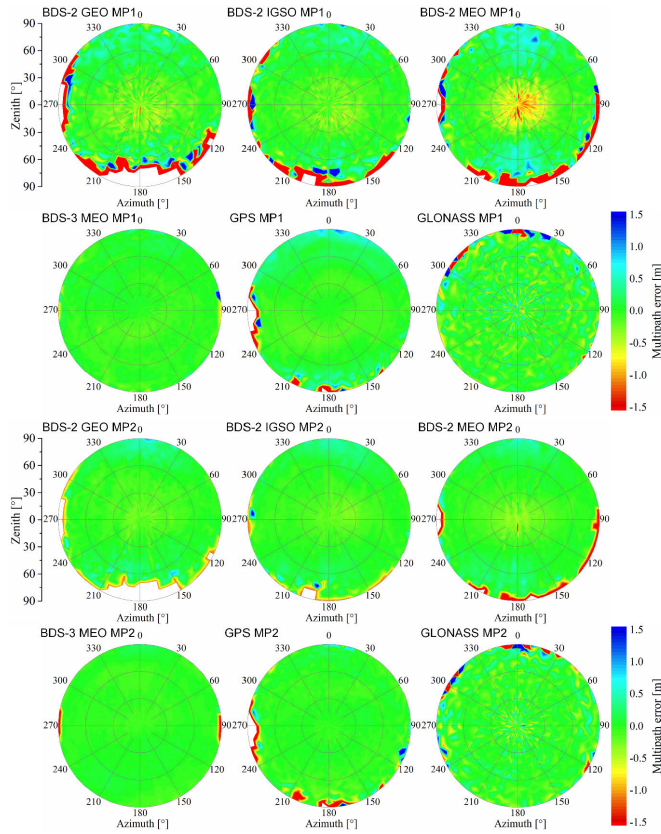


Fig. 6. Azimuth–zenith maps of MP_1/MP_2 for BDS-2 GEO, BDS-2 IGSO, BDS-2 MEO, BDS-3 MEO, GPS, and GLONASS, where the azimuth of 270° represents the flight direction; the mean value is computed based on the noises and multipath errors located in each $2^\circ \times 2^\circ$ bin and the mean values are plotted smoothly in the map; the range of multipath errors is from -1.5 to 1.5 m, and those less than -1.5 m and more than 1.5 m are displayed in pure red and blue, respectively.

but those of BDS-2 deviates from 0 m trendily to different extents for different types of satellites. Most notably, the BDS-2 MEO MP_1 even reaches from -0.5 to -1.0 m. It can be also observed that the BDS-2 MP_2 is much less than BDS-2 MP_1 in the zone with elevation angles above 60° , which is consistent with the average values in Fig. 5. This elevation-dependent multipath error comes from the BDS-2 signal itself instead of the receiver, which has been validated by the past research [32], [33]. Fortunately, BDS-3 satellites have solved this problem, and their multipath errors are also near 0 m in the zone with high elevations, as shown in the figure. For the MP_1 and MP_2 of GLONASS, the bigger multipath errors (reddish bin) alternate with the smaller ones (bluish bin) irregularly in the zone with zenith angles below 30° , but no tendency multipath errors exhibit notably. The reason for the irregular alternation of red and blue bins may be that the noises of GLONASS measurements vary at a large range of ± 12 m, and the available data points used for the average calculation in each $2^\circ \times 2^\circ$ bin are limited, thereby resulting in several large or small MP_1/MP_2 averages in some bins. In the zone with zenith angles above 60° , namely, elevation angles below 30° , some zones with multipath errors of more than 1.5 m (pure red) or less than -1.5 m (pure blue) appear in some maps, especially for BDS-2 GEO MP_1 , BDS-2 IGSO MP_1 , BDS-2 MEO MP_1/MP_2 , and GPS $MP_1/$

TABLE I
POD STRATEGIES FOR THE TJU-1 SATELLITE

Measurement model	
Observations	Ionosphere-free combinations (LC+PC), the weight scale factors for GPS, GLONASS, BDS-3 MEO, BDS-2 MEO, BDS-2 IGSO and BDS-2 GEO satellites are 1.0:1.0:1.0:1.0:1.0:20.0. The weight scale factors for pseudorange and carrier-phase observations are 100.0:1.0
Interval	10 seconds
Data preprocessing	“TurboEdit” [34]+“VAREC” [35] method
POD arc length	30h, 6h overlap arc between adjacent POD arcs
GNSS ephemeris	WHU combined precise orbit and clock products
GNSS PCO and PCV	PCO and PCV model from igs14.atx [36]
Receiver clock offset	An individual clock offset for GPS and the system biases between GPS and GLONASS; an individual clock offset for BDS
LEO PCO and PCV	The nominal offset of ARP to CoM is (+78.00, +72.50, -246.20)mm, PCO and PCV are estimated
LEO attitude	Attitude data transmitted down by the satellite
Dynamical model	
Earth gravity field	EIGEN-6S (150×150) [37], including the time-varying part
N-body gravitation	Moon, Sun and other planets, JPL DE405 [38]
Solid earth tide	IERS Conventions 2010 [39]
Earth pole tide	IERS Conventions 2010 [39]
Ocean tide	FES2004 [40]
Ocean pole tide	IERS Conventions 2010 [39]
Relativistic effects	IERS Conventions 2010 [39]
Atmosphere drag	DTM94 model (density) [41], macro model, piece-wise constant drag coefficients with 60 min intervals
Solar/Earth radiation	Macro model, fixed pressure coefficients
Empirical acceleration	Piece-wise constant empirical acceleration coefficients in the along-track and cross directions with 60min and 360min intervals, respectively
Reference frame	
Coordinate system	ITRF 2014
Precession/nutation	IAU 2006/IAU 2000R06 model
Earth rotation parameters	IERS final EOP products
Estimation Method	
Estimator	Least square
Mode	Batch processing

MP_2 . It demonstrates that the multipath errors at low elevation angles still exist for BDS-2 as the blue values show in Fig. 5, even though their averages are much less than those at high elevation angles.

III. PRECISE ORBIT DETERMINATION

In this contribution, the onboard GPS/GLONASS/BDS data of the TJU-1 satellite from 2022/31 to 2022/37 are processed to determine the satellite orbit. The POD experiments based on single GPS/GLONASS/BDS are carried out. For ease of expression, the GPS-based, GLONASS-based, and BDS-based POD solutions are abbreviated as “G,” “R,” and “C,” respectively. Meanwhile, the PODs based on multi-GNSS fusion are also performed, which have fusions in the form of GPS + GLONASS, GPS + BDS, GLONASS + BDS, and GPS + GLONASS + BDS. In similar, they are abbreviated as “G + R,” “G + C,” “R + C,” and “G + R + C,” respectively. All single-GNSS and multi-GNSS fusion solutions are tested and assessed carefully.

A. POD Strategies

The detailed POD strategies are listed in Table I. The dual-frequency ionosphere-free carrier-phase (LC) and pseudorange

(PC) measurements are used. A method named “VAREC,” which could detect outliers or cycle slips by the statistical test of postresiduals after the estimation of position or interepoch position variation using pseudorange or carrier-phase measurements [34], is adopted together with the commonly used “TurboEdit” method [35] for GNSS data preprocessing to obtain clean observations. The length of a POD arc is 30 h from 21:00 on the previous day to 03:00 on the next day with a 6-h overlap between adjacent arcs. The multi-GNSS products from Wuhan University (WHU), Wuhan, China, are used to compute the precise orbits and clocks of GPS/GLONASS/BDS satellites. Taking into account the ephemeris accuracy of different types of GNSS satellites, the weight scale factors are set as 1.0:1.0:1.0:1.0:1.0:20.0 for GPS, GLONASS, BDS-3 MEO, BDS-2 MEO, IGSO, and GEO satellites. The larger the scale factor, the smaller the weight of observations. The PCO and PCV of GNSS satellites are corrected by using the IGS model from “igs14.atx.” The nominal offset of the antenna reference point (ARP) relative to the center of mass (CoM) of the TJU-1 satellite is provided by the manufacturer. The PCO and PCV parameters of the antenna will be estimated. Various conservative and nonconservative forces are modeled precisely for accurate POD, including the gravity of the Earth, N -body gravitational perturbation, earth and ocean tides, atmospheric drag, and so on. At the same time, the empirical accelerations in the along-track and cross directions, and the atmospheric drag coefficient, are estimated as piecewise constants (PWC) to compensate for the error of modeled forces. Besides, the solar radiation pressure and earth radiation pressure are corrected by a macromodel. At last, the postprocessing POD estimates all parameters by using the least square in the batch mode.

Among these POD strategies, of most concern should be the estimation of drag coefficients and empirical acceleration coefficients. In consideration of the unstable attitude and inaccurate drag coefficients for the small satellite platform, significant errors may exist in the modeled accelerations in the along-track direction due to the complex atmosphere drag. Therefore, in order to make up for this potential deficiency, the drag coefficients and empirical acceleration coefficients in the along-track direction are estimated as PWC every short interval of only 60 min. The setting of 60 min is based on a series of tests and comparisons. Fig. 7 shows the RMS statistics of orbit differences in the radial (R), tangential (T), and normal (N) directions and 3-dimensional (3-D) position over 5 h from 0.5 to 5.5 h of the overlap arc for the GPS-based solution with different intervals for coefficient estimation. It can be seen clearly that the overlapped orbit consistency decreases gradually from 2.85 to 47.22 cm as the interval is increased from 60 to 180 min. It indicates that the interval should not be too long to compensate for the errors in modeled forces. However, a too-short interval of 30 min also leads to poor orbit consistency, as Fig. 7 shows. Hence, the interval of 60 min is regarded as optimal in this research.

In addition, it should be noted that the multi-GNSS fusion could provide abundant observations for POD but also bring new issues, such as the compatibility and interoperability of various GNSS constellations. Fig. 8 shows the differences

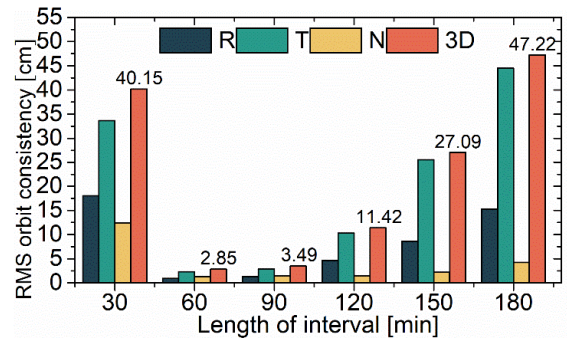


Fig. 7. RMS of overlapped orbit differences as the function of time interval within which the drag coefficient and the tangential empirical acceleration are estimated as constant.

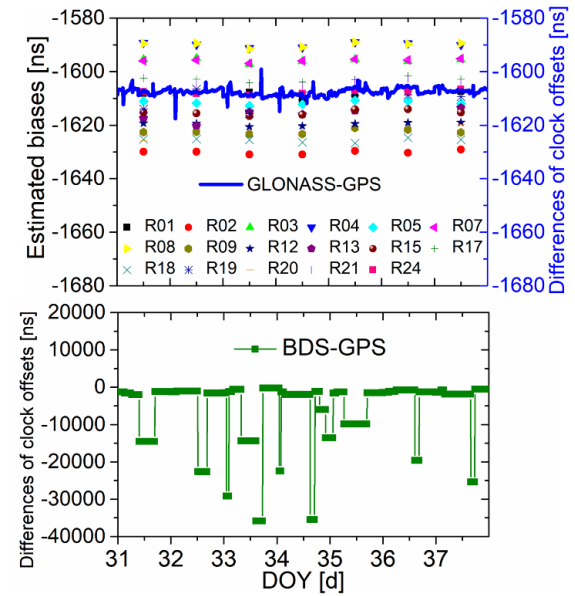


Fig. 8. Differences between receiver clock offsets estimated in GPS-based and GLONASS-based solutions (top, blue line), the estimated bias for each GLONASS satellite on each day (top, dot), and differences between receiver clock offsets estimated in GPS-based and BDS-based solutions (bottom).

between receiver clock offsets estimated in different single-GNSS solutions. It is obvious that there is a significant intersystem bias between GPS and GLONASS, which is essentially the difference between GPS and GLONASS signal delays in the same processing unit. Therefore, for any fusion solution involving GPS and GLONASS, the intersystem bias has to be estimated in addition to the clock offset. Furthermore, in consideration of the frequency division multiple access (FDMA) adopted in GLONASS signal modulation, the bias should be parameterized as a constant for each GLONASS satellite [42]. Fig. 8 also presents the estimated bias for each GLONASS satellite on each day. As can be clearly seen, the variation amplitude of the estimated bias is relatively small from day to day, and satellites with different frequencies show different biases, while satellites with the same frequency exhibit almost the same bias, such as R01 and R05, R03 and R07, and R17 and R21. This result demonstrates the reasonability of intersystem bias estimation. Similarly, the differences between receiver clock offsets estimated in GPS-based and BDS-based solutions are also shown in the bottom panel. Unlike the top one, this difference curve is in the

form of jump, where the difference remains almost constant over an irregular period. Therefore, an individual clock offset parameter for BDS, instead of the intersystem bias, should be estimated in the multi-GNSS fusion solutions involving BDS. It should be noted that this irregular period is due to the special design of the positioning module in the GNSS receiver, where GPS/GLONASS and BDS signals are acquired and tracked in different processing units, and thus, their coarse adjustments to the receiver clock offset are inconsistent.

B. PCO/PCV Estimation

The nominal offset of ARP relative to CoM in the spacecraft-fixed coordinate frame is provided by the satellite manufacturer. However, the actual receiving position of GNSS signals is the antenna phase center (APC), which does not exactly coincide with ARP, and the instantaneous APC (IAPC) also usually changes over time. Therefore, the PCO vector and PCVs, which are defined as the offset of mean APC (MAPC) relative to ARP and the difference between IAPC and MAPC, respectively, are directly estimated to correct the offset of IAPC relative to ARP in the POD processing. The estimation process consists of the following two steps.

- 1) Relevant studies have demonstrated that the PCO parameter in the z -direction of the spacecraft-fixed frame, namely, in the geocentric direction, could be estimated without any conditions, while those in the x - and y -directions are unobservable and estimated usually unstable [43]. Therefore, only the ionosphere-free (LC) PCO of each GNSS in the z -direction is estimated for the TJU-1 satellite. Of course, GLONASS signals are modulated by using the FDMA, which means the frequencies are different for different GLONASS satellites, so the LC PCOs of GLONASS are not estimated. The z -direction PCO is estimated as one parameter per day together with other orbit parameters. The initial value and prior standard deviation (std) of the z -direction PCO are set as 0.0 and 1.0 mm, respectively. The arithmetic mean of estimated PCOs on different days is taken as the final estimate value. Readers are referred to these literatures [43], [44], [45], [46] for more details of the estimation process.
- 2) The residual approach is used to estimate the PCVs on different azimuths and zeniths of the antenna space. First, POD with the final PCO estimate value is conducted to generate a series of posteriori carrier-phase residuals. Then, the antenna space is divided into a grid based on the azimuth and zenith variation. Finally, the arithmetic mean of posteriori carrier-phase residuals within the area near each grid point is regarded as the PCV estimate value of this grid point. Although the residual approach seems simple, it has already been successfully applied to improve the POD of JASON-1 and GRACE-A [47], [48].

Fig. 9 shows the z -direction PCOs of GPS LC and BDS LC for each day over the period from 2022/31 to 2022/37, as well as the mean and std statistics. As can be observed clearly, compared with the estimations of GPS LC PCOs with a mean of -3.30 mm and a std of 2.53 mm, the estimations

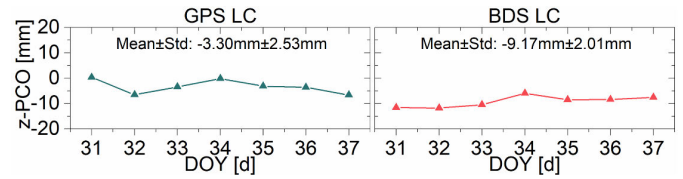


Fig. 9. Estimated PCOs of GPS LC (left) and BDS LC (right) in the z -direction from 2022/31 to 2022/37.

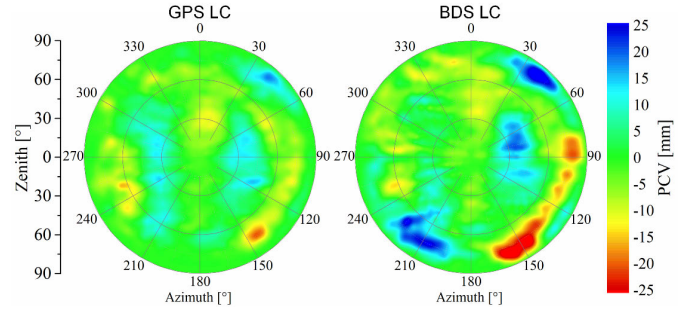


Fig. 10. Azimuth–zenith maps of GPS LC and BDS LC PCVs; the PCVs located in each $2^\circ \times 2^\circ$ bin are plotted smoothly in the map; the range of PCV values is from -25 to 25 mm, and those less than -25 mm and more than 25 mm are displayed in pure blue and red, respectively.

of BDS LC PCOs have a larger mean of -9.17 mm and a smaller std of 2.01 mm. It indicates that the z -PCOs of BDS LC are more obvious and could be estimated more stably in comparison with those of GPS LC . The positioning antenna of the receiver is a micropatch antenna with a thickness of about 2.5 cm. Obviously, the estimated PCOs are within the size range of the antenna. The LC PCVs in each $2^\circ \times 2^\circ$ bin of the antenna azimuth–zenith map are also estimated by using the ionosphere-free carrier-phase postfit residuals. The estimated azimuth–zenith PCV maps of GPS LC and BDS LC are shown in Fig. 10. It can be seen from the figure that the PCVs of GPS LC are within the range of ± 5 mm in most directions, but they could reach up to ± 15 mm in a few directions, such as on the azimuth of 140° – 150° . The PCVs of BDS LC are more obvious than those of GPS LC . In the directions with the azimuth of 30° – 50° , 140° – 165° , and 195° – 225° , the PCVs of GPS LC could reach up to ± 25 mm or even more.

The corrections of PCO/PCV have important influences on the final POD results. The GPS-based and BDS-based POD schemes with the estimated PCO/PCV correction, with PCO but no PCV correction, and without PCO/PCV correction are abbreviated as “GPS_PCO_PCV,” “GPS_PCO_NoPCV,” “GPS_NoPCO_NoPCV,” “BDS_PCO_PCV,” “BDS_PCO_NoPCV,” and “BDS_NoPCO_NoPCV,” respectively. Fig. 11 shows the daily and overall RMS statistics of the R/T/N/3-D orbit differences between these schemes. Comparing “GPS_NoPCO_NoPCV” and “GPS_PCO_NoPCV” shows that the overall RMSs of the R/T/N/3-D orbit differences caused by GPS PCO correction are 0.11, 0.26, 0.04, and 0.29 cm, respectively, while those caused by GPS PCV correction reach up to 0.79, 2.08, 0.32, and 2.25 cm, respectively, if comparing “GPS_PCO_NoPCV” and “GPS_PCO_PCV.” In similar, the comparisons between “BDS_NoPCO_NoPCV,” “BDS_NoPCO_NoPCV,” and “BDS_PCO_PCV” reveal that

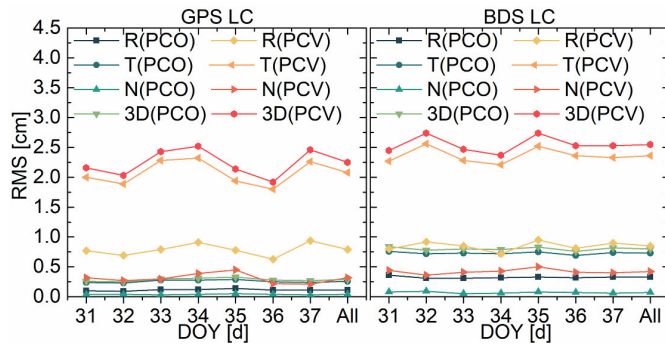


Fig. 11. Influence of PCO/PCV estimation on final orbit results; R(PCO), T(PCO), N(PCO), and 3-D(PCO) represent the RMS statistics of orbit differences between POD results with estimated PCO correction and those without PCO correction; R(PCV), T(PCV), N(PCV), and 3-D(PCV) represent the RMS statistics of orbit differences between POD results with estimated PCV correction and those without PCV correction. “All” represents the overall statistics.

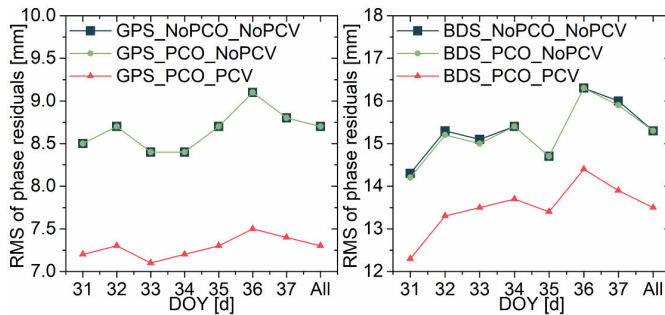


Fig. 12. Daily and overall RMSs of posteriori carrier-phase residuals for different GPS-based (left) and BDS-based (right) POD schemes with or without the estimated PCO/PCV corrections. For the BDS-based POD schemes, only the posteriori carrier-phase residuals of BDS-2 IGSO, BDS-2 MEO, and BDS-3 MEO satellites are counted for the RMS statistics.

the overall RMSs of R/T/N/3-D orbit differences caused by BDS PCO correction are 0.33, 0.73, 0.07, and 0.80 cm, respectively, while those caused by BDS PCV correction are 0.85, 2.36, 0.42, and 2.55 cm, respectively. The PCO and PCV corrections have slightly more notable effects on BDS-based POD orbits than those on GPS-based ones. Fig. 12 shows the daily and overall RMSs of posteriori carrier-phase residuals for different GPS-based and BDS-based solutions further. As can be observed clearly that the posteriori carrier-phase residuals only change a little after the PCO corrections but decrease notably after the PCV corrections. It indicates that the internal consistency of POD orbits is improved significantly after the PCO/PCV correction. In summary, Figs. 11 and 12 have fully demonstrated that the influences of PCO/PCV correction on POD results are not negligible, and the estimation of PCO/PCV is necessary and effective for high-precision POD processing.

C. Accuracy Assessments

It is crucial to assess the final orbit precision and accuracy of POD solutions. The RMS statistics of the overlapped orbit differences of all single-GNSS and multi-GNSS fusion solutions and the orbit differences between them are listed in Table II. The diagonal elements of the table represent the

TABLE II
RMSs OF OVERLAPPED ORBIT DIFFERENCES FOR EACH SOLUTION AND RMSs OF ORBIT DIFFERENCES BETWEEN DIFFERENT SOLUTIONS

RMS [cm]	G	R	C	G+R	G+C	R+C	G+R+C
G	2.18 2.76	6.10 6.75	6.48 7.13	3.61 3.98	4.36 4.81	5.28 5.79	3.93 4.31
R	2.54 1.38	2.78 3.39	7.88 8.68	4.37 4.86	6.67 7.34	5.40 5.91	5.25 5.80
C	2.74 1.17	3.28 1.57	1.75 2.23	6.48 7.14	2.52 2.76	3.05 3.36	3.85 4.23
G+R	1.56 0.60	1.76 1.19	2.77 1.13	1.49 2.07	4.80 5.29	4.66 5.12	2.89 3.17
G+C	1.85 0.81	2.74 1.40	1.06 0.40	2.06 0.84	1.42 1.91	2.53 2.77	2.26 2.48
R+C	2.14 1.03	2.11 1.12	1.33 0.50	1.89 0.93	1.04 0.45	1.42 1.96	2.35 2.58
G+R+C	1.64 0.72	2.11 1.25	1.67 0.61	1.18 0.54	0.98 0.33	0.94 0.46	1.17 1.71

RMS of the overlapped orbit differences in the T direction and 3-D position, while the lower and upper triangle elements represent the overall RMS statistics of the orbit differences between two POD solutions in the R/N directions and the T direction/3-D position, respectively. As can be observed clearly from the diagonal elements that the 3-D overlapped orbit consistency is 2.76, 3.39, and 2.23 cm for the single GNSS solutions of “G,” “R,” and “C,” respectively. If using the orbit results of “G + R + C,” which have the best overlapped orbit consistency of 1.71 cm, as a reference, the 3-D orbit accuracies of “G,” “R,” and “C” are 4.31, 5.80, and 4.23 cm, respectively, as can be seen from the last column in Table II. All these results indicate that the POD precision of all single-GNSS solutions is at an equivalent level, but “G” is slightly worse than “C” and “R” is worse than the other two. This precision performance is consistent with the quality of GPS/GLONASS/BDS observations analyzed above. It can also be seen clearly from Table II that the multi-GNSS fusion solutions achieve significantly better POD precision for the TJU-satellite, compared with the single-GNSS ones. The reason for the improvement is obvious. The multi-GNSS fusion solutions can utilize more GNSS measurements to estimate the orbit parameters with higher accuracy, making up for the relatively poor observation continuity and availability in the case of single-GNSS ones. Especially in those anomalous arcs with GNSS signal disturbance or interruption, as shown in Fig. 3, where orbits are unconstrained by GNSS measurements and computed based on the pure dynamical integration, estimated orbit parameters with higher accuracy from the multi-GNSS fusion solutions can generate the higher precision integral orbits compared to those from single-GNSS ones. Meanwhile, as shown in Table II, the 3-D overlapped orbit consistency in the range of 1.7–2.1 cm also illustrates almost the equivalent precision level for different multi-GNSS fusion solutions. Furthermore, Fig. 13 shows the RMS of posteriori carrier-phase residuals for different types of GNSS satellites in different solutions. The RMSs of the carrier-phase residuals for all IGSO/MEO satellites are at the level of 7–15 mm, which indicates the good consistency between orbit results and GNSS observations, even though they are larger than

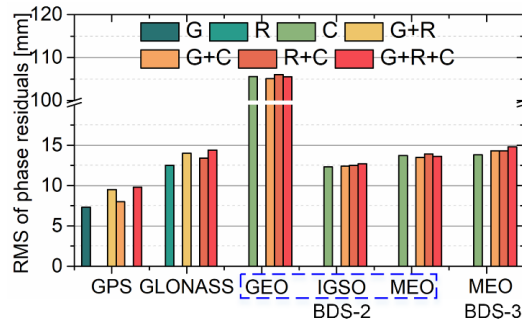


Fig. 13. RMSs of posteriori carrier-phase residuals for different types of GNSS satellites.

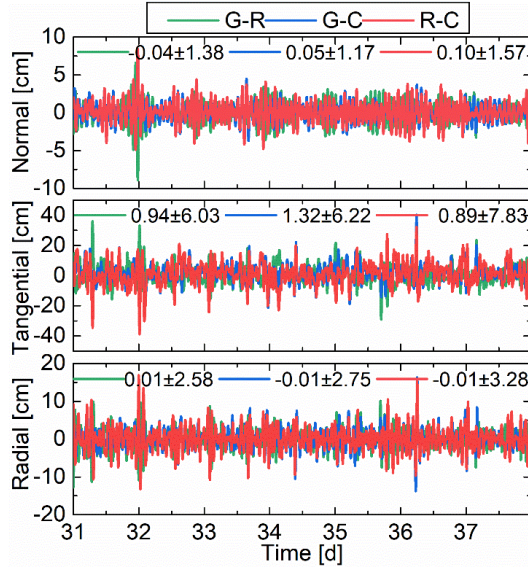


Fig. 14. Orbit differences between three single-GNSS solutions in the radial (bottom), tangential (middle), and normal (top) directions; the mean and std statistics for each error curve are marked in the figure as “mean \pm std.”

100 mm for BDS-2 GEO satellites. These performance indices are comparable to the reported results of some small LEO satellites, such as Luojia-1A and Tianping-1B [23], [26].

Due to the lack of SLR data and external precise orbit products as a reference, it is difficult to assess the external orbit accuracy of each POD solution directly for the TJU-1 satellite. However, even so, it is still possible to infer the approximate orbit accuracy by applying the law of error propagation. Given the 3-D RMS of the differences between any two solutions, RMS_{3D} , and that the precision of a solution is almost at the same level as the other and there is no notable systematic bias between these two solutions, the accuracy of a solution may be inferred to be $RMS_{3D}/\sqrt{2}$. As can be seen from the lower and upper triangle elements of Table II, the orbit difference statistics (RMS) between any two of “G,” “R,” and “C” solutions are in the range of 2.5–3.3, 6.1–7.9, 1.1–1.6, and 6.7–8.7 cm in the *R/T/N* directions and 3-D position, respectively. Meanwhile, Fig. 14 displays the orbit difference curves in the *R/T/N* directions, as well as their mean and std statistics. The *R/T/N* differences vary within the range of ± 10 , ± 20 , and ± 5 cm for most of the time, respectively, and the mean values are close to zero, indicating that the single-GNSS solutions are consistent between each other,

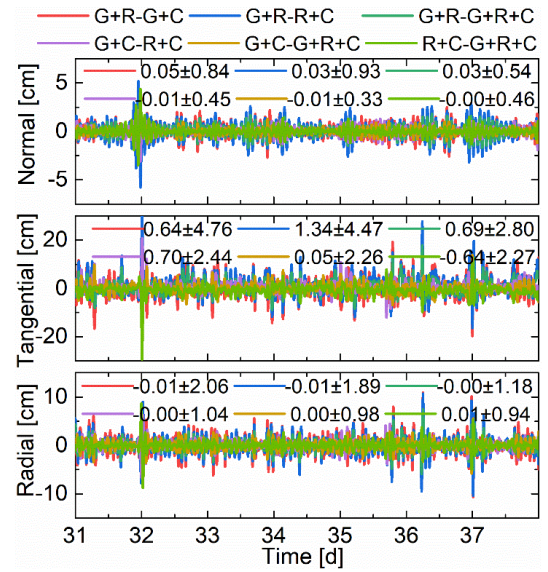


Fig. 15. Orbit differences between four multi-GNSS fusion solutions in the radial (bottom), tangential (middle), and normal (top) directions; the mean and std statistics for each error curve are marked in the figure as “mean \pm std.”

and no noticeable systematic bias exists between different solutions. Therefore, according to Table II and Fig. 14, the accuracy of any single-GNSS solution could be then inferred as about 4.7–6.2 cm ($6.7\text{--}8.7\text{ cm}/\sqrt{2}$), which agrees well with the RMS statistics of 4.2–5.8 cm when a single-GNSS solution is compared to the “G + R + C” solution, as shown in the last column of Table II. In similar, Fig. 15 also shows the orbit differences in the *R/T/N* directions between any two multi-GNSS fusion solutions, and their mean and std values are given in the bracket as well. Obviously, no systematic bias exists between different multi-GNSS fusion solutions, showing the good consistency of all orbit results. In consideration of the orbit difference statistics (3-D RMS) of 2.5–5.3 cm shown in Table II and the good consistencies of orbit results for all multi-GNSS solutions in Fig. 15, the approximate orbit accuracies for the multi-GNSS fusion solutions could be inferred at the level of about 1.7–3.7 cm ($2.5\text{--}5.3\text{ cm}/\sqrt{2}$), which also agrees well with the RMS statistics of 1.7–3.2 cm on the orbit differences between the multi-GNSS solutions and the “G + R + C” solution, as shown in the last column of Table II.

It must be pointed out that the orbit precision and accuracy of TJU-1 are slightly worse than those of some large LEO satellites, such as FY3C, Sentinel-3A, and Sentinel-6A [10], [20], [24], no matter the single-GNSS or multi-GNSS fusion solutions are adopted. There may be several reasons for the slightly worse performance. For example, the ambiguities are not fixed as the precise integers in the current POD strategies. However, the more important factor is probably the poor continuity and availability of GNSS observations during three periods each day when the attitude of the small satellite platform is adjusted with large orientation changes of up to $\pm 70^\circ$, thereby resulting in serious disturbance or even complete interruption for GNSS signal tracking by the miniature receiver. Nevertheless, it is important that the achieved orbit precision and accuracy at the centimeter level are sufficient to

fulfill the requirements of the precise occultation tasks for the small TJU-1 satellite.

IV. SUMMARY AND CONCLUSION

TJU-1 is a small LEO satellite equipped with a miniature GPS/GLONASS/BDS receiver. In this contribution, the quality of the collected GNSS observations from TJU-1 is assessed in terms of the tracking performance, the number of available GNSS satellites, and the pseudorange measurement accuracy. POD experiments based on single GPS/GLONASS/BDS and multi-GNSS fusion are conducted. The results show that the orbit precision of single-GNSS solutions is 2.2–3.4 cm in terms of the overlapped orbit consistency, and their approximate orbit accuracy is inferred to be at the level of about 4.7–6.2 cm according to the orbit differences between different solutions. With multi-GNSS fusion, the precision and inferred accuracy of orbits are improved to 1.7–2.1 cm and about 1.7–3.7 cm, respectively. This performance is slightly worse than the reported results of some large LEO satellites. The main reason is probably the poor continuity and availability of GNSS observations during three periods each day when the attitude of the small satellite platform is adjusted with large orientation changes of up to $\pm 70^\circ$, thereby resulting in serious disturbance or even complete interruption for GNSS signal tracking by the miniature receiver. However, the achieved orbit precision and accuracy are enough to meet the mission requirements of the small TJU-1 satellite.

The experiments on the TJU-1 satellite have fully demonstrated that the centimeter-level POD is achievable for the small LEO satellites using the miniature multi-GNSS receiver. More importantly, the POD precision and accuracy performance could be improved further with multi-GNSS fusion. Along with the rapid development of space and electronic technologies, small LEO satellites have been applied widely in many fields, including communication, earth observation, space remote sensing, and so on [49]. Therefore, the multi-GNSS receiver would have broad application prospects for a wide range of small satellites in the future, in view of its excellent POD performance.

ACKNOWLEDGMENT

The numerical calculations in this article were done on the supercomputing system in the Supercomputing Center of Wuhan University.

REFERENCES

- [1] B. T. Fang and E. Seifert, "An evaluation of global positioning system data for Landsat-4 orbit determination," in *Proc. AIAA Aerosp. Sci. Meeting*, Reno, NV, USA, 1985, p. 286.
- [2] D. B. Goldstein, "Real-time, autonomous, precise orbit determination using the global positioning system," Ph.D. dissertation, Dept. Air Force, Univ. Colorado, Boulder, CO, USA, 2000.
- [3] O. Montenbruck and R. Kroes, "In-flight performance analysis of the CHAMP BlackJack GPS receiver," *GPS Solutions*, vol. 7, no. 2, pp. 74–86, Aug. 2003.
- [4] Z. Kang, B. Tapley, S. Bettadpur, J. Ries, P. Nagel, and R. Pastor, "Precise orbit determination for the GRACE mission using only GPS data," *J. Geodesy*, vol. 80, no. 6, pp. 322–331, Jul. 2006.
- [5] H. Bock et al., "GPS-derived orbits for the GOCE satellite," *J. Geodesy*, vol. 85, no. 11, pp. 807–818, May 2011.
- [6] L. Cerri et al., "Precision orbit determination standards for the Jason series of altimeter missions," *Mar. Geodesy*, vol. 33, pp. 379–418, Aug. 2010.
- [7] M. Bonnedal, J. Christensen, A. Carlström, and A. Berg, "Metop-GRAS in-orbit instrument performance," *GPS Solutions*, vol. 14, no. 1, pp. 109–120, Jan. 2010.
- [8] C. Zhao and X. Tang, "Precise orbit determination for the ZY-3 satellite mission using GPS receiver," *J. Astronaut.*, vol. 34, no. 9, pp. 1202–1206, Sep. 2013.
- [9] J. van den IJssel, J. Encarnação, E. Doornbos, and P. Visser, "Precise science orbits for the swarm satellite constellation," *Adv. Space Res.*, vol. 56, no. 6, pp. 1042–1055, Sep. 2015.
- [10] O. Montenbruck, S. Hackel, and A. Jäggi, "Precise orbit determination of the Sentinel-3A altimetry satellite using ambiguity-fixed GPS carrier phase observations," *J. Geodesy*, vol. 92, no. 7, pp. 711–726, Nov. 2017.
- [11] O. Montenbruck et al., "Tracking and orbit determination performance of the GRAS instrument on MetOp-A," *GPS Solutions*, vol. 12, no. 4, pp. 289–299, Apr. 2008.
- [12] A. Mander and S. Bisnath, "GPS-based precise orbit determination of low Earth orbiters with limited resources," *GPS Solutions*, vol. 17, no. 4, pp. 587–594, Dec. 2012.
- [13] H. Bock, A. Jäggi, G. Beutler, and U. Meyer, "GOCE: Precise orbit determination for the entire mission," *J. Geodesy*, vol. 88, no. 11, pp. 1047–1060, Jul. 2014.
- [14] O. Montenbruck, S. Hackel, J. van den IJssel, and D. Arnold, "Reduced dynamic and kinematic precise orbit determination for the swarm mission from 4 years of GPS tracking," *GPS Solutions*, vol. 22, no. 3, p. 79, Jun. 2018.
- [15] J. Yuan, C. Zhao, and Q. Wu, "Phase center offset and phase center variation estimation in-flight for ZY-3 01 and ZY-3 02 spaceborne GPS antennas and the influence on precision orbit determination," *Acta Geodaetica Cartographica Sinica*, vol. 47, no. 5, pp. 672–682, May 2018.
- [16] K. Shao et al., "Analysis of Tiangong-2 orbit determination and prediction using onboard dual-frequency GNSS data," *GPS Solutions*, vol. 24, no. 1, p. 11, Nov. 2019.
- [17] M. Zrinjski, U. Barković, and K. Matika, "Development and modernization of GNSS," *Geodetski List*, vol. 73, no. 1, pp. 45–65, 2019.
- [18] J. J. K. Parker, F. H. Bauer, B. W. Ashman, J. J. Miller, W. Enderle, and D. Blonski, "Development of an interoperable GNSS space service volume," in *Proc. 31st Int. Tech. Meeting Satell. Division Inst. Navigat. (ION GNSS)*, Miami, FL, USA, Oct. 2018, pp. 1246–1256.
- [19] X. Chen, S. Zhao, M. Wang, and M. Lu, "Space-borne BDS receiver for LING QIAO satellite: Design, implementation and preliminary in-orbit experiment results," *GPS Solutions*, vol. 20, no. 4, pp. 837–847, Oct. 2015.
- [20] M. Li et al., "Precise orbit determination of the Fengyun-3C satellite using onboard GPS and BDS observations," *J. Geodesy*, vol. 91, no. 11, pp. 1313–1327, Apr. 2017.
- [21] X. Li, T. Ma, W. Xie, K. Zhang, J. Huang, and X. Ren, "FY-3D and FY-3C onboard observations for differential code biases estimation," *GPS Solutions*, vol. 23, no. 2, p. 57, Apr. 2019.
- [22] L. Wang, R. Chen, B. Xu, B. Zhang, T. Li, and C. Wu, "The challenges of LEO based navigation augmentation system—Lessons learned from Luojia-1A satellite," in *Proc. China Satell. Navigat. Conf. (CSNC)*, Beijing, China, 2019, pp. 298–310.
- [23] X. Zhao et al., "High-precision orbit determination for a LEO nanosatellite using BDS-3," *GPS Solutions*, vol. 24, no. 4, p. 102, Aug. 2020.
- [24] O. Montenbruck, S. Hackel, M. Wermuth, and F. Zangerl, "Sentinel-6A precise orbit determination using a combined GPS/Galileo receiver," *J. Geodesy*, vol. 95, no. 9, p. 109, Sep. 2021.
- [25] X. Li et al., "Precise orbit determination for the FY-3C satellite using onboard BDS and GPS observations from 2013, 2015, and 2017," *Engineering*, vol. 6, no. 8, pp. 904–912, Aug. 2020.
- [26] L. Wang et al., "Centimeter-level precise orbit determination for the Luojia-1A satellite using BeiDou observations," *Remote Sens.*, vol. 12, no. 12, p. 2063, Jun. 2020.
- [27] M. N. Sweeting, "Modern small satellites-changing the economics of space," *Proc. IEEE*, vol. 106, no. 3, pp. 343–361, Mar. 2018.
- [28] D. Gu, Y. Liu, B. Yi, J. Cao, and X. Li, "In-flight performance analysis of MEMS GPS receiver and its application to precise orbit determination of APOD-A satellite," *Adv. Space Res.*, vol. 60, no. 12, pp. 2723–2732, Dec. 2017.
- [29] W. Schreiner, C. Rocken, S. Sokolovskiy, and D. Hunt, "Quality assessment of COSMIC/FORMOSAT-3 GPS radio occultation data derived from single- and double-difference atmospheric excess phase processing," *GPS Solutions*, vol. 14, no. 1, pp. 13–22, Jul. 2009.

- [30] X. Gong et al., "Precise real-time navigation of the small TJU-1 satellite using GPS, GLONASS and BDS," *Measurement*, vol. 204, Nov. 2022, Art. no. 112090.
- [31] R. Mu, Y. Dang, and C. Xu, "BDS-3/GNSS data quality and positioning performance analysis," in *Proc. China Satell. Navigat. Conf. (CSNC)*, Chengdu, China, 2020, pp. 368–379.
- [32] A. Hauschild, O. Montenbruck, J.-M. Sleewaegen, L. Huisman, and P. J. G. Teunissen, "Characterization of compass M-1 signals," *GPS Solutions*, vol. 16, no. 1, pp. 117–126, Feb. 2011.
- [33] L. Wanninger and S. Beer, "BeiDou satellite-induced code pseudorange variations: Diagnosis and therapy," *GPS Solutions*, vol. 19, no. 4, pp. 639–648, Nov. 2014.
- [34] F. Wang and J. Liu, "A new algorithm detecting cycle slips in satellite-borne GPS carrier phase measurements for precise orbit determination," *Geomatics Inf. Sci. Wuhan Univ.*, vol. 29, no. 9, pp. 772–774, Sep. 2014.
- [35] G. Blewitt, "An automatic editing algorithm for GPS data," *Geophys. Res. Lett.*, vol. 17, no. 3, pp. 199–202, Mar. 1990.
- [36] P. Rebischung and R. Schmid, "IGS14/IGS14. ATX: A new framework for the IGS products," Presented at the AGU Fall Meeting, 2016.
- [37] C. Forste et al., "A new release of EIGEN-6: The latest combined global gravity field model including LAGEOS, GRACE and GOCE data from the collaboration of GFZ Potsdam and GRGS Toulouse," in *Proc. EGU Gen. Assem.*, Vienna, Austria, 2012, p. 2821.
- [38] L. V. Morrison and D. W. Evans, "Check on JPL DE405 using modern optical observations," *Astron. Astrophys. Suppl. Ser.*, vol. 132, no. 3, pp. 381–386, May 1998.
- [39] G. Petit and B. Luzum, "IERS conventions," Verlag des Bundesamts für Kartographie und Geodäsie, Frankfurt, Germany, IERS Tech. Note 36, 2010.
- [40] F. Lyard, F. Lefevre, T. Letellier, and O. Francis, "Modelling the global ocean tides: Modern insights from FES2004," *Ocean Dyn.*, vol. 56, nos. 5–6, pp. 394–415, Sep. 2006.
- [41] C. Berger, R. Biancale, F. Barlier, and M. Ill, "Improvement of the empirical thermospheric model DTM: DTM94—A comparative review of various temporal variations and prospects in space geodesy applications," *J. Geodesy*, vol. 72, no. 3, pp. 161–178, Mar. 1998.
- [42] X. Zuo, X. Jiang, P. Li, J. Wang, M. Ge, and H. Schuh, "A square root information filter for multi-GNSS real-time precise clock estimation," *Satell. Navigat.*, vol. 2, no. 1, p. 28, Dec. 2021.
- [43] D. Gu, Y. Lai, J. Liu, B. Ju, and J. Tu, "Spaceborne GPS receiver antenna phase center offset and variation estimation for the Shiyao 3 satellite," *Chin. J. Aeronaut.*, vol. 29, no. 5, pp. 1335–1344, Oct. 2016.
- [44] O. Montenbruck, M. Garcia-Fernandez, Y. Yoon, S. Schön, and A. Jäggi, "Antenna phase center calibration for precise positioning of LEO satellites," *GPS Solutions*, vol. 13, no. 1, pp. 23–34, Jun. 2008.
- [45] A. Jäggi, R. Dach, O. Montenbruck, U. Hugentobler, H. Bock, and G. Beutler, "Phase center modeling for LEO GPS receiver antennas and its impact on precise orbit determination," *J. Geodesy*, vol. 83, no. 12, pp. 1145–1162, Jul. 2009.
- [46] J. Tu, D. Gu, Y. Wu, and D. Yi, "Phase residual estimations for PCVs of spaceborne GPS receiver antenna and their impacts on precise orbit determination of GRACE satellites," *Chin. J. Aeronaut.*, vol. 25, no. 4, pp. 631–639, Aug. 2012.
- [47] B. Haines, Y. Bar-Sever, W. Bertiger, S. Desai, and P. Willis, "One-centimeter orbit determination for Jason-1: New GPS-based strategies," *Mar. Geodesy*, vol. 27, nos. 1–2, pp. 299–318, Jan. 2004.
- [48] B. Haines et al., "Space-based satellite antenna maps; impact of different satellite antenna maps on LEO & terrestrial results," in *Proc. IGS Workshop*, Miami, FL, USA, 2008.
- [49] J. R. Kopacz, R. Herschitz, and J. Roney, "Small satellites an overview and assessment," *Acta Astronaut.*, vol. 170, pp. 93–105, May 2020.



Xingxing Li received the B.Sc. degree from the School of Geodesy and Geomatics, Wuhan University, Wuhan, China, in 2008, and the Ph.D. degree from the Department of Geodesy and Remote Sensing, German Research Center for Geosciences (GFZ), Potsdam, Germany, in 2015.

He is currently a Professor at Wuhan University and is mainly interested in GNSS precise data processing and its application for geosciences.



Pengcheng Wang received the B.S. and M.S. degrees in electronic information engineering and electronic science and technology from the Changchun University of Science and Technology, Changchun, China, in 2010 and 2013, respectively.

He is currently with the Tianjin Yunyao Aerospace Technology Company, Ltd., Tianjin, China. He is currently a System Engineer. His research interests include satellite navigation and GNSS-RO.



Qingyun Wang received the B.Sc. degree from the School of Geodesy and Geomatics, Wuhan University, Wuhan, China, in 2020, where she is currently pursuing the master's degree.

Her area of research currently focuses on satellite navigation, LEO real-time orbit determination, and multi-GNSS precise orbit determination.



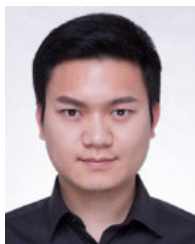
Fuhong Wang received the Ph.D. degree in geodesy and engineering surveying from the School of Geodesy and Geomatics, Wuhan University, Wuhan, China, in 2006.

He is currently a Professor at Wuhan University. His current research focuses on satellite navigation and satellite orbit determination.



Jizhang Sang received the Ph.D. degree in satellite navigation from the Queensland University of Technology, Brisbane, Australia, in 1997.

He joined Wuhan University as a Professor of Geodesy and Navigation in 2013 through China's "The Thousand Talents Plan." His research interests include satellite/debris orbit mechanics, space tracking, conjunction analysis, space geodesy, and satellite navigation.



Xuewen Gong received the B.S., M.S., and Ph.D. degrees from Wuhan University, Wuhan, China, in 2012, 2015, and 2020, respectively.

He is currently a Postdoctoral Researcher with the School of Geodesy and Geomatics, Wuhan University. He is leaving Wuhan University to work at the National Time Service Center, Chinese Academy of Sciences, Xi'an, China. He is mainly working on precise orbit determination of LEO satellites, autonomous navigation of GNSS satellites, and GNSS/LEO integrated precise orbit determination.



Shuaihe Gao received the bachelor's degree from Harbin Engineering University, Harbin, China, in 2012.

He is a Professor with National Time Service Center, Chinese Academy of Sciences, Xi'an, China. He is mainly working on satellite navigation, satellite communication, and spatial time-frequency technology.